Scattering coefficients of superconducting microwave resonators. I. Transfer matrix approach

Qi-Ming Chen,[1,2,*] Meike Pfeiffer,[2] Matti Partanen,[1] Florian Fesquet,[1,2] Kedar E. Honasoge,[1,2] Fabian Kronowetter,[1,2] Yuki Nojiri,[1,2] Michael Renger,[1,2] Kirill G. Fedorov,[1,2] Achim Marx,[1] Frank Deppe,[1,2,3,†] and Rudolf Gross[1,2,3,‡]

[1]*Walther-Meißner-Institut, Bayerische Akademie der Wissenschaften, 85748 Garching, Germany*

[2]*Physik-Department, Technische Universität München, 85748 Garching, Germany*

[3]*Munich Center for Quantum Science and Technology (MCQST), Schellingstr. 4, 80799 Munich, Germany*

(Received 22 February 2022; revised 22 November 2022; accepted 28 November 2022; published 9 December 2022)

We describe a unified classical approach for analyzing the scattering coefficients of superconducting microwave resonators with a variety of geometries. To fill the gap between experiment and theory, we also consider the influences of small circuit asymmetry and the finite length of the feedlines, and describe a procedure to correct their influences in typical experiments. We show that, similar to the transmission coefficient of a hanger-type resonator, the reflection coefficient of a necklace- or cross-type resonator also contains a so-called reference point that can be used to characterize the internal quality factor of the resonator. Our results provide a comprehensive understanding of superconducting microwave resonators from the design concepts to the characterization details.

DOI: 10.1103/PhysRevB.106.214505

I. INTRODUCTION

Superconducting microwave resonators are ubiquitously used in superconducting quantum circuits [1]. Owing to the high flexibility of circuit design, the resonators can be made and coupled to other components, or an external circuitry, in various ways with different emphases [2]. For example, a necklace-type resonator, where the feedline(s) and the resonator are coupled end to end, is often used to control and couple different qubits [3–16], while a hanger-type resonator, where one end of the bare resonator is side coupled to a feedline, is more common for reading out the quantum information [17–28]. Depending on the detailed geometry of the circuit, the scattering coefficients of superconducting microwave resonators can show vastly different line shapes that carry the information of different physical processes. However, in contrast to the well-studied hanger-type $\lambda/4$ resonator [29–38], the existing studies of the necklace-type resonator are often restricted to its transmission response [39–41]. The reflection coefficients of the necklace-type resonator are rarely discussed [42,43] and its importance has fallen into neglect. As a consequence, it is well known that the transmission coefficient is sufficient to characterize a hanger-type resonator, which contains a reference point that distinguishes the internal and external quality factors from the line shape [44–48]. However, to date one still has to combine the transmission measurements with either detailed cable calibration or finite-element simulations to characterize a necklace-type resonator [39–41,49–51]. This complexity limits not only the reliability of the characterization results but also the applicability of the necklace-type resonators to a complex circuit.

Here, and also in a parallel paper [52], we study the scattering coefficients of superconducting microwave resonators in either classical or quantum perspectives. In this work, we employ the transfer matrix method in microwave engineering and derive analytically the scattering coefficients of a general resonator [53]. We observe the existence of reference point in the reflection coefficient of the necklace- and cross-type resonators, which can be used to characterize the internal quality factor. We also explore the physical origin of the line-shape distortions that are commonly seen in experiments, and describe a procedure to remove these imperfections step by step. Finally, we experimentally demonstrate the existence of the reference point in a necklace-type resonator, and illustrate the correction procedures for the distorted line shape. These results provide a systematic study of the scattering coefficients of superconducting microwave resonators in the classical perspective.

The rest of this paper is organized as follows: In Sec. II, we introduce the circuit diagrams of different types of superconducting microwave resonators, and review their electrical properties such as resonant frequency and quality factors. Next, we outline the transfer-matrix method and derive the ideal scattering coefficients of different resonators in Sec. III. We study how the circuit asymmetries and a finite length of feedline can influence the measurement spectrum in Sec. IV, and obtain a general description of a practical scattering spectrum. We demonstrate these observations in an experiment in Sec. V, and we conclude this study in Sec. VI. Detailed derivations of the scattering coefficients for different types of resonators can be found in Appendixes A–E. A detailed procedure for correcting the distortions in practical measurements is described in Appendix F. Throughout this study, we assume that the frequency range of interest is around the resonance frequency of the fundamental mode by default.

*qiming.chen@wmi.badw.de
†frank.deppe@wmi.badw.de
‡rudolf.gross@wmi.badw.de

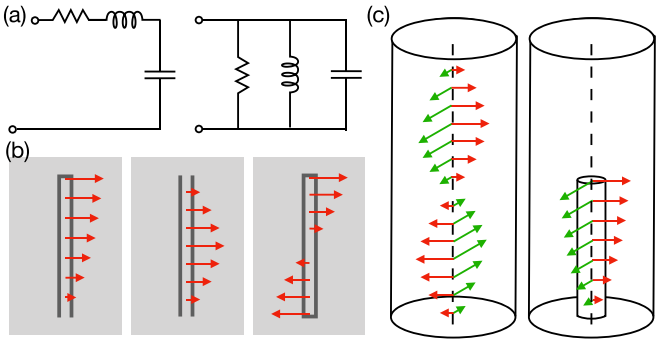

FIG. 1. Schematics of several different microwave resonators. (a) In lumped-element circuits, the series (left) and parallel (right) RLC resonant circuits are the two fundamental types of microwave resonators. (b) In distributed-element circuits, there are three types of transmission-line resonators: the short-circuited $\lambda/4$ (left), the short-circuited $\lambda/2$ (middle), and the open-circuited $\lambda/2$ (right) resonators. (c) Microwave resonators can be also made by bulky 3D devices, which can be modeled by a short-circuited $\lambda/2$ (left) or a short-circuited $\lambda/4$ (right) transmission-line resonator. In all the panels, red and green vectors depict the spatial modes of the resonator, which are determined by the boundary conditions.

II. CIRCUIT DESCRIPTION OF MICROWAVE RESONATORS

In lumped-element circuits, there are two general types of circuit diagrams that can be modeled as a *zero*-dimensional microwave resonator. As schematically shown in Fig. 1(a), the first one is called the series RLC resonator with the following input impedance:

$$Z_{\rm s} = R_{\rm s} + j\omega L_{\rm s} + \frac{1}{j\omega C_{\rm s}}. \tag{1}$$

Here, $R_{\rm s}$, $L_{\rm s}$, and $C_{\rm s}$ are the resistance, inductance, and capacitance of the circuit, j is the imaginary unit that follows the convention of electrical engineering. The resonance occurs at $\mathrm{Im}(Z_{\rm s}) = 0$, which corresponds to a resonant frequency $\omega_0 = 1/\sqrt{L_{\rm s}C_{\rm s}}$ and a (internal) quality factor $Q_{\rm i} = \omega_0 L_{\rm s}/R_{\rm s} = 1/(\omega_0 R_{\rm s}C_{\rm s})$ [53]. The second circuit, as shown in Fig. 1(b), is called the parallel RLC resonator with an input impedance of

$$Z_{\rm p} = \left(\frac{1}{R_{\rm p}} + \frac{1}{j\omega L_{\rm p}} + j\omega C_{\rm p}\right)^{-1}. \tag{2}$$

Similarly, one can calculate the resonance frequency and the (internal) quality factor as $\omega_0 = 1/\sqrt{L_{\rm p}C_{\rm p}}$ and $Q_{\rm i} = R_{\rm p}/(\omega_0 L_{\rm p}) = \omega_0 R_{\rm p}C_{\rm p}$, respectively [53].

In comparison, a finite length of transmission line with proper boundary conditions can be also described as a microwave resonator in 1D. Depending on the load impedance $Z_{\rm L}$ and the length l, the input impedance of a transmission line can be written as [53]

$$Z(l) = Z_0 \frac{Z_{\rm L} + Z_0 \tanh \gamma l}{Z_0 + Z_{\rm L} \tanh \gamma l}. \tag{3}$$

Here, $\gamma = \alpha + j\beta$ is the complex propagation constant of the microwave field, Z_0 is the characteristic impedance of the transmission line. By assuming a small damping rate of the transmission line, i.e., $\alpha l \ll 1$, and confining our discussion in a small frequency range around the resonant frequency, i.e., $|\Delta| \ll \omega_0$ with $\Delta = \omega - \omega_0$, we obtain three types of microwave resonators as shown in Fig. 1(b). They are (i) the short-circuited $\lambda/4$ resonator with

$$Z_{\lambda/4} = \frac{Z_0}{\alpha l + j\pi\Delta/2\omega_0} \text{ and } \omega_0 = \frac{\pi v_{\rm ph}}{2l}, \tag{4}$$

(ii) the short-circuited $\lambda/2$ resonator with

$$Z^{(\rm short)}_{\lambda/2} = Z_0(\alpha l + j\pi\Delta/\omega_0) \text{ and } \omega_0 = \frac{\pi v_{\rm ph}}{l}, \tag{5}$$

and (iii) the open-circuited $\lambda/2$ resonator with

$$Z^{(\rm open)}_{\lambda/2} = \frac{Z_0}{\alpha l + j\pi\Delta/\omega_0} \text{ and } \omega_0 = \frac{\pi v_{\rm ph}}{l}. \tag{6}$$

Here, $v_{\rm ph} = \omega/\beta$ is the phase velocity of the propagating microwave field in the transmission line.

Comparing these results with the two lumped-element resonators, we observe that the short-circuited $\lambda/4$ resonator and the open-circuited $\lambda/2$ resonator are equivalent to a parallel RLC resonator with $R_{\rm p} = Z_0/(\alpha l)$, $L_{\rm p} = 1/(\omega_0^2 C)$, and $C_{\rm p} = \pi/(4\omega_0 Z_0)$ or $C_{\rm p} = \pi/(2\omega_0 Z_0)$, respectively. The short-circuited $\lambda/2$ resonator is equivalent to a series RLC resonator with $R_{\rm s} = Z_0\alpha l$, $L_{\rm s} = \pi Z_0/(2\omega_0)$, and $C_{\rm s} = 1/(\omega_0^2 L)$. However, the (internal) quality factor has the same definition for all the three resonators: $Q_{\rm i} = \beta/(2\alpha)$, where $\beta \approx 2\pi/\lambda$. Here, the approximation originates from the fact that ω is close but not exactly the same as ω_0 in the frequency range of interest.

The above discussions also apply to three-dimensional (3D) microwave resonators as shown in Fig. 1(c), which attract an increasing amount of interests during the past decades for their superior quality factors. The inner surface of a 3D resonator naturally defines the voltage nodes of the spatial modes of the electrical field, while the antinodes are located either at the antinodes of the standing waves inside the cavity [54–64], or at the top of a $\lambda/4$-long waveguide pillar standing in the inner space [65–68]. If the electrical fields can be fairly described as one-dimensional (1D) functions of the coordinator, the two types of 3D resonators can be equivalently described by a shorted-circuited $\lambda/2$ or a shorted-circuited $\lambda/4$ transmission-line resonator, respectively. In this regard, we do not distinguish coplanar waveguide resonators and 3D resonators in the current discussion. A careful distinction may be necessary when studying exotic resonator designs, for example, the 2D resonators introduced in Refs. [69,70].

III. IDEAL SCATTERING COEFFICIENTS OF MICROWAVE RESONATORS

To measure the electrical properties of a microwave resonator, such as the resonant frequency and the quality factor, one has to couple it to an external circuitry (i.e., the load) and measure the scattering coefficients, as schematically shown in Figs. 2(a)–2(c). However, the coupling also leads to an inevitable change in the electrical properties to be measured. By convention, we define the loaded quality factor $Q_{\rm l}$ as a combination of two terms [53]

$$\frac{1}{Q_{\rm l}} = \frac{1}{Q_{\rm i}} + \frac{1}{Q_{\rm e}}. \tag{7}$$

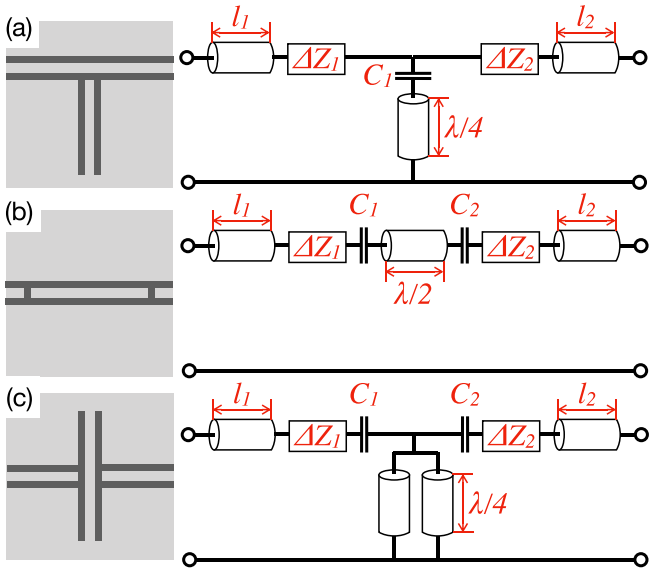

FIG. 2. Schematics of three typical resonator designs and the corresponding circuit diagrams. They are (a) the hanger-type $\lambda/4$ resonator, (b) the necklace-type $\lambda/2$ resonator, and (c) the cross-type $\lambda/2$ resonator. In all the panels, we denote l_1 and l_2 as the lengths of the feedlines that are coupled to the resonator, C_1 and C_2 the coupling capacitors, and ΔZ_1 and ΔZ_2 the circuit asymmetries. Without loss of generality, we label the left and right ports by 1 and 2.

Here, Q_e is defined as the external quality factor which describes the power-loss ratio induced by the external circuity, Q_i is the internal quality factor that characterizes the bare resonator loss. In this section, we study the ideal scattering coefficients of three types of resonators that are commonly seen in superconducting quantum circuits. We assume *zero*-length transmission feedlines, i.e., $l_1, l_2 = 0$, and *zero*-circuit asymmetries, $\Delta Z_1, \Delta Z_2 = 0$, for now for simplicity.

A. Hanger-type λ/4 resonator

The hanger-type $\lambda/4$ resonator is a short-circuited transmission line with one end shorted to ground and the other side coupled to a 1D waveguide. The schematic of this type of resonator is shown in Fig. 2(a), where we define the coupling capacitance as C_1, and label the left and right ports as port 1 and 2, respectively. Following the standard transfer matrix method in microwave engineering [53], the elements of the transfer matrix can be obtained as $A = D = 1$, $B = 0$, and $C = 1/Z$ with $Z = 1/j\omega C_1 + Z_{\lambda/4}$. Here, the convention is chosen such that

$$V_1 = AV_2 + BI_2, \tag{8}$$

$$I_1 = CV_2 + DI_2, \tag{9}$$

where V_1, I_1 and V_2, I_2 are the voltage and current at port 1 and 2, respectively. We note that the positive direction of the currents is pointing from port 1 to 2. Following the standard procedure, the scattering coefficients can be readily calculated with the following recipe [53]:

$$S_{11} = \frac{A + B/Z_0 - CZ_0 - D}{A + B/Z_0 + CZ_0 + D}, \tag{10}$$

$$S_{12} = \frac{2(AD - BC)}{A + B/Z_0 + CZ_0 + D}, \tag{11}$$

$$S_{21} = \frac{2}{A + B/Z_0 + CZ_0 + D}, \tag{12}$$

$$S_{22} = \frac{-A + B/Z_0 - CZ_0 + D}{A + B/Z_0 + CZ_0 + D}. \tag{13}$$

To simplify the expressions, let us consider first a lossless resonator. Knowing that the resonance occurs at $\mathrm{Im}(Z) = 0$, we can calculate the resonant frequency as

$$\omega_r \approx \omega_0 - \frac{2Z_0C_1\omega_0^2}{\pi}. \tag{14}$$

This result still holds for lossy resonators as long as $Q_i \gg \sqrt{Q_e}$, where

$$Q_e = \frac{\pi}{2\omega_r^2 Z_0^2 C_1^2}. \tag{15}$$

This requirement can be seen by inserting ω_r into Eq. (4) while requesting that αl is negligibly small compared to $j\pi\Delta/(2\omega_0)$. It is valid for typical experimental situations in superconducting quantum circuits. In this regard, we rewrite the input impedance of the vertical branch close to the resonant frequency as $Z \approx Z_0 Q_e[1/(2Q_i) + j\delta]$ with $\delta = (\omega - \omega_r)/\omega_r$. Inserting this result into Eqs. (10)–(13), we obtain an analytical form of the scattering coefficients

$$S_{11} = S_{22} \approx -\frac{Q_l/Q_e}{1 + j2Q_l\delta}, \tag{16}$$

$$S_{21} = S_{12} \approx 1 - \frac{Q_l/Q_e}{1 + j2Q_l\delta}. \tag{17}$$

The physical meaning of the parameter Q_e can be understood in the perspective of the Norton's equivalent lumped-element circuit [71–75]. Assuming that $\omega_0 C_1 Z_0 \ll 1$, the loaded quality factor can be written as

$$Q_l = \omega_r C_p \left(\frac{1}{R_p} + \frac{\omega_r^2 Z_0 C_1^2}{2}\right)^{-1}. \tag{18}$$

For $\lambda/4$ resonators, we have $\omega_r C_p \approx \pi/4Z_0$, such that the external quality factor is $Q_e = \pi/(2Z_0^2\omega_r^2 C_1^2)$. Thus, the parameter Q_e defined in Eq. (15) can be interpreted as the external quality factor of a hanger-type $\lambda/4$ resonator, as is indicated in the notation.

The above discussion can be also generalized to a hanger-type $\lambda/2$ resonator. If one neglects the coupling between the open end of the resonator and the ground plane, the scattering coefficients of a hanger-type $\lambda/2$ resonator are exactly the same with those of a hanger-type $\lambda/4$ resonator, as shown in Eqs. (16) and (17). However, the resonant frequency $\omega_r \approx \omega_0 - Z_0 C_1 \omega_0^2/\pi$ is defined differently from those of an $\lambda/4$ resonator. Because adding a coupling capacitor C_1 to the bare resonator does not change the total inductance of the system, we have

$$(C_p + C_1)\omega_r^2 = C_p\omega_0^2 = 1/L_p. \tag{19}$$

It indicates that $\omega_r = [1 + C_1/(2C_p)]\omega_0$ for $C_1 \ll C_p$. Considering the length difference between a $\lambda/4$ and a $\lambda/2$ resonator, the total capacitance of the latter is two times larger than the former and causes a smaller frequency shift. Similarly, one

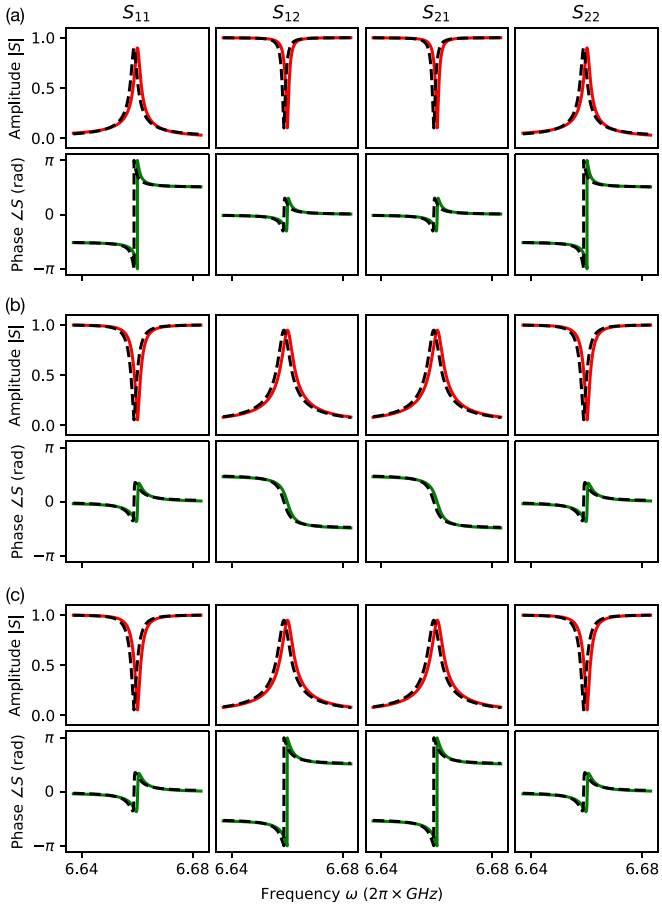

FIG. 3. Simulated scattering coefficients of the three types of microwave resonators shown in Fig. 2. They are (a) the hanger-type $\lambda/4$ resonator, (b) the necklace-type $\lambda/2$ resonator, and (c) the cross-type $\lambda/2$ resonator. In all the panels, the black dashed curves represent the analytical results. They fit closely to the red and green curves, which are the numerical results calculated by using the transfer matrices. The shift between the dashed and solid curves is around $2\pi \times 1$ MHz, which is due to the approximation error of the resonant frequency ω_r. This shift can be removed by calculating ω_r in an iterative manner. In these examples, one extra iteration decreases the shift to $2\pi \times 4$ kHz.

can verify that the external quality factor of a $\lambda/2$ resonator is $Q_e = \pi/(\omega_r^2 Z_0^2 C_1^2)$ by considering a two-times larger total capacitance in the Norton's equivalent lumped-element circuit.

As a crosscheck of the above results, we compare in Fig. 3(a) the analytical formulas with the numerically simulated scattering coefficients of a hanger-type $\lambda/4$ resonator. The numerical simulation is performed by multiplying the transfer matrices of different circuit components at different frequencies. The parameters are chosen as $\alpha = 5.0 \times 10^{-3}$ m^{-1}, $v_{ph} = 1.35 \times 10^8$ m/s, $l = 5.0 \times 10^{-3}$ m, and $Z_0 = 50\ \Omega$, which give $\omega_0 = 2\pi \times 6.75$ GHz, $Q_i = 31\,416$ for a bare $\lambda/4$ resonator. In the presence of the coupling capacitance, $C_1 = 1.0 \times 10^{-14}$ F, the analytical formulas in Eqs. (16) and (17) predict the resonant frequency $\omega_r = 2\pi \times 6.659$ GHz, and the quality factors $Q_e = 3589$, $Q_l = 3221$. These values exhibit an excellent fit to the numerical simulation results.

B. Necklace-type $\lambda/2$ resonator

The necklace-type resonator, as schematically shown in Fig. 2(b), consists of an open-circuited transmission line which is capacitively coupled to two feedlines through the capacitors C_1 and C_2 at the two ends, respectively. The elements of the transfer matrix for the coupling capacitors read as $A = D = 1, B = 1/j\omega C_1$ or $B = 1/j\omega C_2$, and $C = 0$. They are $A = D = \cosh \gamma l, B = Z_0 \sinh \gamma l$, and $C = (1/Z_0) \sinh \gamma l$ for a bare open-circuited $\lambda/2$ resonator. Following a similar treatment as for the hanger-type resonators, we obtain the scattering coefficients as (see Appendix A for details)

$$S_{11} \approx 1 - \frac{2Q_l/Q_{e,1}}{1 + j2Q_l\delta}, \tag{20}$$

$$S_{21} = S_{12} \approx \frac{2Q_l/\sqrt{Q_{e,1}Q_{e,2}}}{1 + j2Q_l\delta}, \tag{21}$$

$$S_{22} \approx 1 - \frac{2Q_l/Q_{e,2}}{1 + j2Q_l\delta}. \tag{22}$$

Here, $1/Q_e = 1/Q_{e,1} + 1/Q_{e,2}$ with

$$Q_{e,k} = \frac{\pi}{2\omega_r^2 Z_0^2 C_k^2},\ k = 1, 2. \tag{23}$$

The resonant frequency is

$$\omega_r = \omega_0 - \frac{Z_0(C_1 + C_2)\omega_0^2}{\pi}. \tag{24}$$

The physical meaning of the parameter Q_e can be also understood in the perspective of the Norton's equivalent lumped-element circuit [76,77]. Assuming that $\omega_0 C_1 Z_0, \omega_0 C_2 Z_0 \ll 1$, the loaded quality factor reads as

$$Q_l = \omega_r C_p \left(\frac{1}{R_p} + \omega_r^2 Z_0 C_1^2 + \omega_r^2 Z_0 C_2^2 \right)^{-1}, \tag{25}$$

where $\omega_r C_p = \pi/2Z_0$ for a $\lambda/2$ resonator. In this regard, the external quality factor can be written as

$$\frac{1}{Q_e} = \frac{2\omega_r^2 Z_0^2 C_1^2}{\pi} + \frac{2\omega_r^2 Z_0^2 C_2^2}{\pi}, \tag{26}$$

which is exactly the sum of the two parameters $1/Q_{e,1}$ and $1/Q_{e,2}$ defined in Eq. (23).

We note that the transmission coefficient S_{21} in Eq. (21) is consistent with the results reported in the literature [39–41]. However, the reflection coefficients S_{11} and S_{22} in Eqs. (20) and (22) are rarely discussed in the literature except Refs. [42,43]. They have an important feature: The complex scattering coefficients form a circle which intersects with the real axis at a fixed point $(1 + j0)$ for $\delta \to \infty$. The circle radius r_c equals to $Q_l/(2Q_e)$ for $C_1 = C_2$. When $C_1 \neq C_2$, the circle radii should be $Q_l/Q_{e,1}$ and $Q_l/Q_{e,2}$ for S_{11} and S_{22}, respectively. These results are similar to the transmission coefficients of a hanger-type resonator. For simplicity, we assume a symmetric resonator geometry, with $Q_{e,1} = Q_{e,2} = 2Q_e$, by default until further notice. The above discussion can be also generalized to a necklace-type $\lambda/4$ resonator, which is a single-port device with only the reflection coefficient shown in Eq. (20). The same formula can be traced back to Ref. [42], which is the cornerstone of the characterization experiments performed in Refs. [67,68] (see also Ref. [48] for

a summary of $\lambda/4$ resonators). Here, the resonant frequency and the external quality factor are $\omega_r \approx \omega_0 - 2Z_0C_1\omega_0^2/\pi$ and $Q_e = \pi/(4\omega_r^2 Z_0^2 C_1^2)$, respectively.

We also compare the analytical formulas with the numerically simulated scattering coefficients of a necklace-type $\lambda/2$ resonator, as shown in Fig. 3(b). Similarly, the numerical simulation is performed by multiplying the transfer matrices of different circuit components at different frequencies, and the parameters are set identical to Fig. 3(a) except that the length of the transmission line is doubled, $l = 1.0 \times 10^{-2}$ m, and a second coupling capacitor, $C_2 = 1.0 \times 10^{-14}$ F, is added. The bare resonator properties, benchmarked by ω_0 and Q_i, are exactly the same as before. However, with the coupling to the external circuitry the analytical formulas in Eqs. (20)–(22) predict the resonant frequency $\omega_r = 2\pi \times 6.659$ GHz, and the quality factors $Q_e = 1795$ and $Q_l = 1698$. These values are in excellent agreement with those obtained by the numerical simulation. We note that if we couple the same $\lambda/2$ resonator to a 1D waveguide in a hanger geometry, we obtain much larger quality factors as $Q_e = 7082$ and $Q_l = 5779$. This is mainly due to the fact that a necklace-type resonator is coupled to the outside circuitry via two coupling capacitors C_1 and C_2, which double the energy dissipation rate.

C. Cross-type λ/2 resonator

There is a third type of superconducting microwave resonator which is rare in coplanar waveguide designs but common in 3D structures. The schematic is shown in Fig. 2(c), where the two ends of the feedlines are coupled to the voltage antinodes of the bare resonator. Here, we restrict our discussion to the fundamental mode of a shorted-circuited $\lambda/2$ resonator, and figuratively name it a cross-type $\lambda/2$ resonator. The circuit diagram is a combination of the hanger- and necklace-type resonators, which consists of two coupling capacitors, C_1 and C_2, and also two parallel short-circuited $\lambda/4$ resonators in the vertical branch. The elements of the transfer matrix read as $A = 1 + 2/(j\omega C_1 Z_{\lambda/4})$, $B = -[j\omega(C_1 + C_2)Z_{\lambda/4} + 2]/(\omega^2 C_1 C_2 Z_{\lambda/4})$, $C = 2/Z_{\lambda/4}$, and $D = 1 + 2/(j\omega C_2 Z_{\lambda/4})$. The scattering coefficients can be readily obtained by following the standard procedure (see Appendix B for details)

$$S_{11} \approx 1 - \frac{2Q_l/Q_{e,1}}{1 + j2Q_l\delta}, \tag{27}$$

$$S_{21} = S_{12} \approx -\frac{2Q_l/\sqrt{Q_{e,1}Q_{e,2}}}{1 + j2Q_l\delta}, \tag{28}$$

$$S_{22} \approx 1 - \frac{2Q_l/Q_{e,2}}{1 + j2Q_l\delta}, \tag{29}$$

where $1/Q_e = 1/Q_{e,1} + 1/Q_{e,2}$ with

$$Q_{e,k} = \frac{\pi}{2\omega_r^2 Z_0^2 C_k^2}, \; k = 1, 2. \tag{30}$$

The resonance occurs at

$$\omega_r = \omega_0 - \frac{Z_0\omega_0^2(C_1 + C_2)}{\pi}. \tag{31}$$

Comparing with Eqs. (20)–(22), the scattering coefficients of a cross-type resonator have an almost identical form as a necklace-type resonator except for a π-phase difference in the transmission coefficients S_{12} and S_{21}. To show this difference, we also numerically calculate scattering coefficients of a cross-type $\lambda/2$ resonator and compare them with the analytical formulas, as shown in Fig. 3(c). Here, the parameters are set identical to Fig. 3(b), such that all the bare-resonator properties are the same. When considering also the coupling, the analytical formulas in Eqs. (27) and (28) predict the resonant frequency $\omega_r = 2\pi \times 6.659$ GHz, and the quality factors $Q_e = 1795$, $Q_l = 1698$. These values are identical to those of a necklace-type $\lambda/2$ resonator.

IV. PRACTICAL DISTORTIONS IN SCATTERING COEFFICIENTS

A. Influence of small circuit asymmetry

In contrast to the ideal cases described above, asymmetries often exist in real circuits in the form of mutual inductance [45], impedance mismatch [46], etc. In this section, we keep the *zero*-length feedline assumption but study the influence of a small circuit asymmetry on the scattering coefficients.

1. Hanger-type resonators

As schematically shown in Fig. 2(a), we consider small circuit asymmetries ΔZ_1, $\Delta Z_2 \ll Z_0$ on both sides of the ideal system. The elements of the transfer matrix with asymmetry can be written as $A = 1 + \Delta Z_1/Z$, $B = \Delta Z_1 + \Delta Z_2 + \Delta Z_1\Delta Z_2/Z$, $C = 1/Z$, $D = 1 + \Delta Z_2/Z$. Following the derivation in Appendix C, we obtain the scattering coefficients as

$$S_{11} \approx -\frac{Q_l'/Q_e'}{1 + j2Q_l\delta}, \tag{32}$$

$$S_{21} = S_{12} \approx 1 - \frac{Q_l'/Q_e'}{1 + j2Q_l'\delta}, \tag{33}$$

$$S_{22} \approx -\frac{Q_l'/Q_e'}{1 + j2Q_l\delta}. \tag{34}$$

Because of the asymmetry, the loaded quality factor becomes $1/Q_l' = 1/Q_i + 1/Q_e'$, where $Q_e' = Q_e Z_0(1/Z_1 + 1/Z_2)/2$ with $Z_1 = Z_0 + \Delta Z_1$ and $Z_2 = Z_0 + \Delta Z_2$. In this regard, both Q_l' and Q_e' can take complex values which indicate a loss mechanism different from a simple exponential energy decay. However, for small circuit asymmetries the real parts of Z_1 and Z_2 should still be dominant. We follow the convention and redefine the loaded quality factor as $1/Q_l' = 1/Q_i + \mathrm{Re}(1/Q_e')$ [45,46]. The information of the imaginary part, $\mathrm{Im}(1/Q_e')$, is interpreted as a small phase factor $\phi = -\arctan[\mathrm{Im}(Q_e')/\mathrm{Re}(Q_e')]$, which rotates the ideal circle by $e^{j\phi}$. With this definition, we rewrite the scattering coefficients as

$$S_{11} \approx -\frac{e^{j\phi}Q_l'/|Q_e'|}{1 + j2Q_l'\delta}, \tag{35}$$

$$S_{21} = S_{12} \approx 1 - \frac{e^{j\phi}Q_l'/|Q_e'|}{1 + j2Q_l'\delta}, \tag{36}$$

$$S_{22} \approx -\frac{e^{j\phi}Q_l'/|Q_e'|}{1 + j2Q_l'\delta}. \tag{37}$$

In what follows, we denote the expression of Q_l' and $1/\mathrm{Re}(1/Q_e')$ as the formal definition of the loaded and external quality factor.

2. Necklace- and cross-type resonators

For the necklace-type resonator shown in Fig. 2(b), the elements of the transfer matrix with asymmetry can be written as

$$A = A_0 + \sinh\gamma l\left(\frac{\Delta Z_1}{Z_0}\right),$$
$$B = B_0 + \sinh\gamma l\left(\frac{\Delta Z_1\Delta Z_2}{Z_0} + \frac{\Delta Z_1}{j\omega C_2 Z_0} + \frac{\Delta Z_2}{j\omega C_1 Z_0}\right) + \cosh\gamma l(\Delta Z_1 + \Delta Z_2),$$
$$C = C_0,$$
$$D = D_0 + \sinh\gamma l\left(\frac{\Delta Z_2}{Z_0}\right),$$

where we denote the transfer matrix elements of the symmetric necklace-type resonator as A_0, B_0, C_0, and D_0. Following the derivation in Appendix D and using the conventional definition $1/Q_l' = 1/Q_i + \mathrm{Re}(1/Q_e')$, we obtain the scattering coefficients as

$$S_{11} \approx 1 - \frac{e^{j\phi_1}2Q_l'/|Q_{e,1}'|}{1 + j2Q_l'\delta}, \tag{38}$$

$$S_{21} = S_{12} \approx \frac{e^{j\phi}2Q_l'/\sqrt{|Q_{e,1}'||Q_{e,2}'|}}{1 + j2Q_l'\delta}, \tag{39}$$

$$S_{22} \approx 1 - \frac{e^{j\phi_2}2Q_l'/|Q_{e,2}'|}{1 + j2Q_l'\delta}. \tag{40}$$

Here, the external quality factor is defined as $1/Q_e' = 1/Q_{e,1}' + 1/Q_{e,2}'$ with $Q_{e,1}' = Q_{e,1}Z_0/Z_1$ and $Q_{e,2}' = Q_{e,2}Z_0/Z_2$. The corresponding phases are $\phi = (\phi_1 + \phi_2)/2$, $\phi_1 = -\arctan[\mathrm{Im}(Q_{e,1}')/\mathrm{Re}(Q_{e,1}')]$, and $\phi_2 = -\arctan[\mathrm{Im}(Q_{e,2}')/\mathrm{Re}(Q_{e,2}')]$.

The above results apply also to a cross-type resonator, as shown in Fig. 2(c), but with a π-phase difference in the transmission coefficients. The scattering coefficients read as (see Appendix E for details)

$$S_{11} \approx 1 - \frac{e^{j\phi_1}2Q_l'/|Q_{e,1}'|}{1 + j2Q_l'\delta}, \tag{41}$$

$$S_{21} = S_{12} \approx -\frac{e^{j\phi}2Q_l'/\sqrt{|Q_{e,1}'||Q_{e,2}'|}}{1 + j2Q_l'\delta}, \tag{42}$$

$$S_{22} \approx 1 - \frac{e^{j\phi_2}2Q_l'/|Q_{e,2}'|}{1 + j2Q_l'\delta}. \tag{43}$$

In these regards, we conclude that a small circuit asymmetry leads to a small rotation of the ideal scattering-response circle in the complex plane. For the transmission coefficients of a hanger-type resonator or the reflection coefficients of a necklace- or cross-type resonator, this rotation is centered at the reference point $(1 + j0)$ with an angle ϕ. This property can be used to correct the distortions caused by the circuit asymmetry in a measured scattering spectrum. We note that the assumption of small asymmetry, $\Delta Z_1, \Delta Z_2 \ll Z_0$, is required to guarantee $\phi \ll \pi$, and thus to justify the assumption $\mathrm{Im}(1/Q_e') \ll \mathrm{Re}(1/Q_e')$ when defining the external quality factor of an asymmetric circuit. The equations described above may also apply to a general circuit with a relatively large impedance mismatch as long as $\phi \ll \pi$. For example, it is reported in Ref. [45] that a ± 10-Ω impedance mismatch on the two sides of a necklace-type $\lambda/2$ resonator leads to $\phi \approx 0.06\pi$, which justifies the general applicability of the understanding that circuit asymmetry causes a rotation around the reference point.

B. Influence of the finite-length feedlines

Aside from circuit asymmetry, a finite length of the microwave feedlines can also influence the measurement result, as shown in Figs. 2(a)–2(c). We recall the expression of the incident and reflected voltages at the position z of a transmission line as [53]

$$V^{\pm}(z) = V_0^{\pm}e^{\mp\gamma z}, \tag{44}$$

where the $\pm$ sign distinguishes the incident and reflected wave propagations, and $V_0^{\pm}$ are the corresponding voltage amplitudes at $z = 0$. For finite values of l_1 and l_2, the incident and reflected voltages transferred through the feedlines $V_1^{\pm\prime}$ and $V_2^{\pm\prime}$ can be described as

$$V_1^{\pm\prime} = e^{\pm\gamma l_1}V_1^{\pm},\ V_2^{\pm\prime} = e^{\pm\gamma l_2}V_2^{\pm}. \tag{45}$$

Here, we denote $V_1^{\pm}$ and $V_2^{\pm}$ as the voltage amplitudes at the sample input and output. The scattering coefficients measured through the feedlines are thus

$$S_{11}' = e^{-2\gamma_1 l_1}S_{11}, \tag{46}$$

$$S_{21}' = e^{-(\gamma_1 l_1 + \gamma_2 l_2)}S_{21}, \tag{47}$$

$$S_{12}' = e^{-(\gamma_1 l_1 + \gamma_2 l_2)}S_{12}, \tag{48}$$

$$S_{22}' = e^{-2\gamma_2 l_2}S_{22}, \tag{49}$$

where we have assumed a perfect impedance match between the feedlines and the sample. A mismatched feedline causes a circuit asymmetry, which contributes to a small local rotation $e^{j\phi}$, as discussed in the previous section.

Under the high-frequency and low-loss approximation of the transmission feedlines, α is a small constant and $\beta = \omega/v_{ph}$ [53]. This reveals that the finite-length feedlines can cause a damping coefficient A and a frequency-dependent phase factor $e^{-j\omega\tau}$ in the scattering coefficients. Here, τ is a constant. In addition, there may also exist a constant phase delay $e^{-j\varphi}$ because of the imperfect calibration of the cable delay. It can be also attributed to the circuit asymmetry, where a global phase factor was neglected in the previous section under the small asymmetry assumption.

In total, we obtain a general model that describes the transmission coefficient of a hanger-type resonator or the reflection coefficient of a necklace- or cross-type resonator

$$S(\omega) \approx Ae^{-j(\omega\tau+\varphi)}\left(1 - \frac{e^{j\phi}Q_l/Q_e}{1 + 2jQ_l(\omega/\omega_r - 1)}\right). \tag{50}$$

This formula describes the scattering coefficients of a single resonator to be measured in real experiments. Similar expressions have been widely used in the literature for characterizing the hanger-type resonators [44–48]. Here, the global factor $Ae^{-j(\omega\tau+\varphi)}$ originates from the finite length of the feedlines, while the local phase $e^{j\phi}$ from the circuit asymmetry. In the complex plane, the former rotates the circle of the ideal scattering coefficients around the original point $(0 + j0)$, which is accompanied with a shrink of the circle radius. The latter

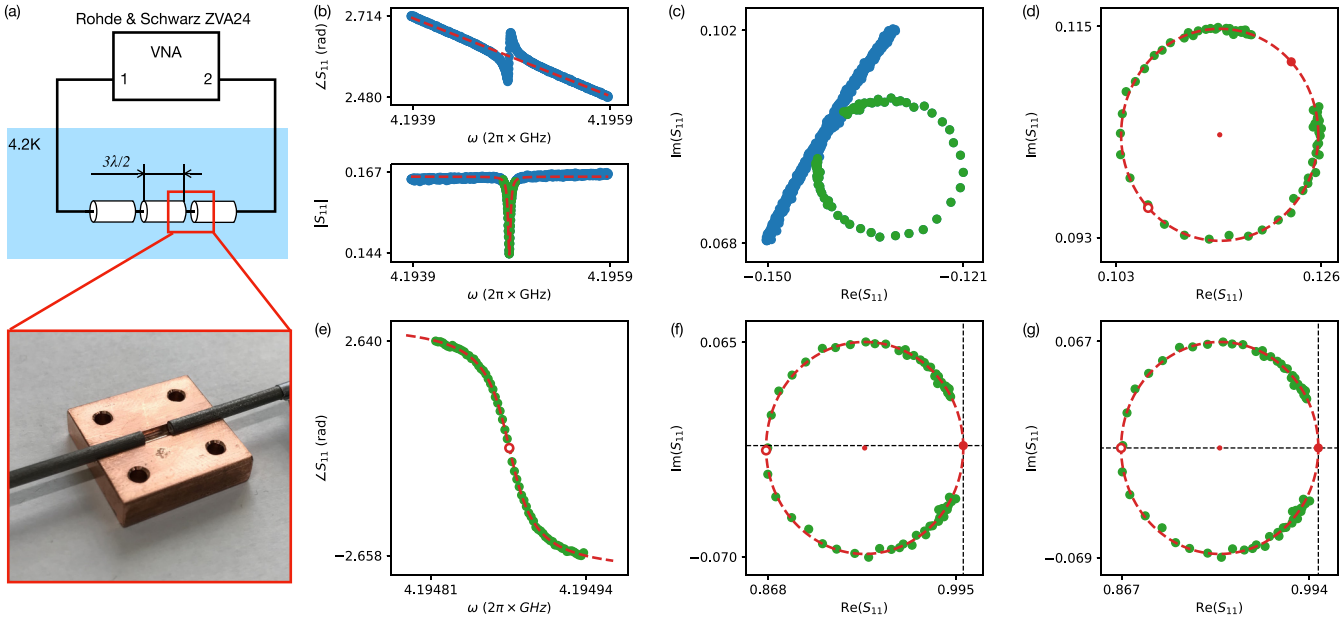

FIG. 4. (a) Sketch of the experimental setup. Here, a necklace-type transmission-line resonator is coupled to the feedlines with two mechanically tunable coupling capacitors. (b)–(g) The step-by-step correction procedure for the measured reflection coefficient S_{11} for the third harmonic mode. In specifics, (b) and (c) show the raw data. The blue dots represent the whole data set, from which the green dots are selected for characterization. The latter is chosen within ± 2 times of the FWHM around the resonant frequency. (d), (f), (g) Show the data after removing the frequency-dependent phase shift, the global constant phase shift and attenuation, and the local constant phase shift, respectively. (e) Shows the procedure to identify the resonance point, which is shown as the open red dot in (d)–(g). Detail of the correction procedure can be found in Appendix F.

causes a rotation around the reference point $(1 + j0)$ with a second but slight shrink of the circle radius.

We emphasize that Eq. (50) applies to a general necklace-type resonator even with unequal coupling capacitances C_1 and C_2. Knowing the existence of the reference point, one can eliminate the prefactors $Ae^{-j(\omega\tau+\varphi)}$ and $e^{j\phi}$ in Eq. (50) and recover the ideal reflection responses given by Eqs. (20) and (22). Here, the loaded quality factor Q_l can be conveniently extracted from the full width at half-maximum (FWHM) of the line shapes and should be independent of the measurements S_{11} and S_{22}. In the complex plane, the measurement data form two independent circles with radii $Q_\mathrm{l}/Q_{\mathrm{e},1}$ and $Q_\mathrm{l}/Q_{\mathrm{e},2}$, respectively. One therefore obtains the total external quality factor from the simple equation $1/Q_\mathrm{e} = 1/Q_{\mathrm{e},1} + 1/Q_{\mathrm{e},2}$, and consequently the internal quality factor $1/Q_\mathrm{i} = 1/Q_\mathrm{l} - 1/Q_\mathrm{e}$ (see Appendix F for a concrete example).

V. EXPERIMENTAL RESULTS

With the understandings of distortion in a general scattering spectrum, we perform a prototypical experiment to characterize a necklace-type resonator by measuring only the reflection coefficient. The experimental setup is schematically shown in Fig. 4(a). Here, the resonator consists of a commercial NbTi transmission line with length $l \simeq 81$ mm, which is capacitively coupled to two feedlines through the small gaps with a customizable distance d. In our experiment, we focus on the third harmonic mode of the resonator, and measure the reflection coefficient S_{11} with a fixed gap size $d \simeq 1.5$ mm. The raw data, i.e., the amplitude, phase, and complex value of $S_{11}(\omega)$, are shown in Figs. 4(b) and 4(c), respectively. Following the recipe described in Appendix F, we correct the influence of the finite feedlines and the circuit asymmetry sequentially and retrieve the ideal scattering coefficients, as shown in Figs. 4(d)–4(g). We obtain the resonant frequency and the loaded, internal, and external quality factors as $\omega_{3\mathrm{r}} = 2\pi \times 4.195$ GHz, $Q_{3\mathrm{l}} = 133\,856$, $Q_{3\mathrm{i}} = 154\,454$, and $Q_{3\mathrm{e}} = 1\,003\,690$. Here, the quality factors $Q_{3\mathrm{l}}$, $Q_{3\mathrm{i}}$, $Q_{3\mathrm{e}}$ are defined for the third harmonic mode, which are different from those of the fundamental mode. The loaded quality factor for the nth mode is defined as $1/Q_{\mathrm{nl}} = 1/Q_{\mathrm{ni}} + 1/Q_{\mathrm{ne}}$, with the internal and external quality factors being, ideally,

$$Q_{\mathrm{ni}} = \frac{n\pi}{2\alpha l} = nQ_\mathrm{i}, \tag{51}$$

$$Q_{\mathrm{ne}} = \frac{n\pi}{2\omega_{\mathrm{nr}}^2 Z_0^2 \left(C_1^2 + C_2^2\right)} = \frac{Q_\mathrm{e}}{n}. \tag{52}$$

This result is consistent with that obtained by the conventional method, which requires both the transmission and reflection measurements. We note that this method is also used in another experiment, which characterizes the internal quality factors of two coupled necklace-type resonators with only reflection measurements [78].

VI. CONCLUSIONS AND OUTLOOK

In conclusion, we provide a comprehensive study of the scattering coefficients of superconducting microwave resonators in the classical perspective. By using the transfer matrix method, we derive the analytical expressions of the scattering coefficients with different circuit geometries, such as hanger, necklace, and cross type. We also discuss the phys-

ical origin of the distortions that are commonly seen in a measurement spectrum, which include the circuit asymmetry and the finite length of the feedlines. These understandings open a door to correct the experimental imperfections step by step, resume the ideal spectrum, and characterize the electrical properties of a general microwave resonator. It is shown that, similar to the transmission coefficient of a hanger-type resonator, the reflection coefficient of a necklace- or cross-type resonator also contains a reference point that can be used to characterize the internal quality factor of the resonator. We demonstrate this observation in experiment and observe an excellent fit among the analytical, numerical, and experimental results.

The experimental data and the Python codes for generating and analyzing the data of this study are available online [79].

ACKNOWLEDGMENT

We acknowledge support by German Research Foundation via Germany's Excellence Strategy (Grant No. EXC-2111-390814868), Elite Network of Bavaria through the program ExQM, European Union via the Quantum Flagship project QMiCS (Project No. 820505), German Federal Ministry of Education and Research via the project QuaRaTe (Project No. 13N15380).

APPENDIX A: SCATTERING COEFFICIENTS OF A NECKLACE-TYPE λ/2 RESONATOR

As introduced in Sec. III B, the transfer matrix of a necklace-type $\lambda/2$ resonator reads as

$$A = \cosh\gamma l + \frac{\sinh\gamma l}{j\omega C_1 Z_0},$$
$$B = \sinh\gamma l\left(Z_0 - \frac{1}{\omega^2 C_1 C_2 Z_0}\right) + \cosh\gamma l\left(\frac{1}{j\omega C_1} + \frac{1}{j\omega C_2}\right), \tag{A1}$$

$$C = \frac{\sinh\gamma l}{Z_0}, \quad D = \cosh\gamma l + \frac{\sinh\gamma l}{j\omega C_2 Z_0}. \tag{A2}$$

Correspondingly, we obtain the scattering coefficients as

$$S_{11} = \frac{(2j\omega Z_0 C_2 + 1)e^{\gamma l} + (2j\omega Z_0 C_1 - 1)e^{-\gamma l}}{(2j\omega Z_0 C_1 + 1)(2j\omega Z_0 C_2 + 1)e^{\gamma l} - e^{-\gamma l}}, \tag{A3}$$

$$S_{21} = \frac{-4\omega^2 Z_0^2 C_1 C_2}{(2j\omega Z_0 C_1 + 1)(2j\omega Z_0 C_2 + 1)e^{\gamma l} - e^{-\gamma l}}, \tag{A4}$$

$$S_{22} = \frac{(2j\omega Z_0 C_1 + 1)e^{\gamma l} + (2j\omega Z_0 C_2 - 1)e^{-\gamma l}}{(2j\omega Z_0 C_1 + 1)(2j\omega Z_0 C_2 + 1)e^{\gamma l} - e^{-\gamma l}}, \tag{A5}$$

where $S_{12} = S_{21}$. For open-circuited $\lambda/2$ resonators, we define $\beta l = \pi + \pi\Delta/\omega_0$ and $\alpha l = \pi/(2Q_i)$, and assume that the frequency of interest, i.e., ω, is very close to the bare resonant frequency ω_0. Thus, the above equations can be simplified as

$$S_{11} \approx \frac{\left(\frac{1}{Q_i} - \frac{2\omega Z_0(C_2-C_1)\Delta}{\omega_0}\right) + j\left(\frac{2\omega Z_0(C_1+C_2)}{\pi} + \frac{2\Delta}{\omega_0}\right)}{\left(\frac{1}{Q_i} - \frac{4\omega^2 Z_0^2 C_1 C_2}{\pi} - \frac{2\omega Z_0(C_1+C_2)\Delta}{\omega_0}\right) + j\left(\frac{2\omega Z_0(C_1+C_2)}{\pi} + \frac{2\Delta}{\omega_0}\right)}, \tag{A6}$$

$$S_{21} \approx \frac{\frac{4\omega^2 Z_0^2 C_1 C_2}{\pi}}{\left(\frac{1}{Q_i} - \frac{4\omega^2 Z_0^2 C_1 C_2}{\pi} - \frac{2\omega Z_0(C_1+C_2)\Delta}{\omega_0}\right) + j\left(\frac{2\omega Z_0(C_1+C_2)}{\pi} + \frac{2\Delta}{\omega_0}\right)}, \tag{A7}$$

$$S_{22} \approx \frac{\left(\frac{1}{Q_i} - \frac{2\omega Z_0(C_1-C_2)\Delta}{\omega_0}\right) + j\left(\frac{2\omega Z_0(C_1+C_2)}{\pi} + \frac{2\Delta}{\omega_0}\right)}{\left(\frac{1}{Q_i} - \frac{4\omega^2 Z_0^2 C_1 C_2}{\pi} - \frac{2\omega Z_0(C_1+C_2)\Delta}{\omega_0}\right) + j\left(\frac{2\omega Z_0(C_1+C_2)}{\pi} + \frac{2\Delta}{\omega_0}\right)}. \tag{A8}$$

Similar to the analysis in the hanger-type resonator, the coupled resonant frequency ω_r is obtained by setting the imaginary part of the denominator to *zero*. This gives

$$\omega_r \approx \omega_0 - \omega_0^2 Z_0(C_1 + C_2)/\pi, \tag{A9}$$

where we have assumed that $\omega_r \approx \omega_0$. A more precise form is

$$\omega_r \approx \omega_0 - \omega_0\omega_r Z_0(C_1 + C_2)/\pi, \tag{A10}$$

where ω_r can be solved iteratively. Inserting this relation into the above equations, we obtain

$$S_{11} \approx \frac{\frac{1}{Q_i} + \frac{2\omega^2 Z_0^2(C_2^2 - C_1^2)}{\pi} + j2\delta}{\left(\frac{1}{Q_i} + \frac{2\omega^2 Z_0^2(C_1^2+C_2^2)}{\pi}\right) + j2\delta},$$
$$S_{21} \approx \frac{4\omega^2 Z_0^2 C_1 C_2}{\left(\frac{1}{Q_i} + \frac{2\omega^2 Z_0^2(C_1^2+C_2^2)}{\pi}\right) + j2\delta},$$
$$S_{22} \approx \frac{\frac{1}{Q_i} + \frac{2\omega^2 Z_0^2(C_1^2 - C_2^2)}{\pi} + j2\delta}{\left(\frac{1}{Q_i} + \frac{2\omega^2 Z_0^2(C_1^2+C_2^2)}{\pi}\right) + j2\delta}. \tag{A11}$$

Here, we have used the assumption that $\omega \approx \omega_r$. Using again the assumption that ω, ω_0, and ω_r are close to each other, and replacing ω in the numerator by ω_0, we obtain Eqs. (20)–(22) in the main text.

APPENDIX B: SCATTERING COEFFICIENTS OF A CROSS-TYPE λ/2 RESONATOR

As introduced in Sec. III C, the transfer matrix of a cross-type $\lambda/2$ resonator reads as

$$A = 1 + \frac{2(\alpha\lambda/4 + j\pi\Delta/2\omega_0)}{j\omega C_1 Z_0},$$
$$B = -\frac{2(\alpha\lambda/4 + j\pi\Delta/2\omega_0)}{\omega^2 C_1 C_2 Z_0} + \left(\frac{1}{j\omega C_1} + \frac{1}{j\omega C_2}\right), \tag{B1}$$
$$C = \frac{2(\alpha\lambda/4 + j\pi\Delta/2\omega_0)}{Z_0},$$
$$D = 1 + \frac{2(\alpha\lambda/4 + j\pi\Delta/2\omega_0)}{j\omega C_2 Z_0}. \tag{B2}$$

Correspondingly, we write the scattering coefficients as

$$S_{11} = \frac{j\omega(C_1+C_2)Z_0 + 2(\alpha\lambda/4 + j\pi\Delta/2\omega_0)\left[1 + j\omega(C_2-C_1)Z_0 + \omega^2 C_1C_2Z_0^2\right]}{[-2\omega^2C_1C_2Z_0^2 + j\omega(C_1+C_2)Z_0] + 2(\alpha\lambda/4 + j\pi\Delta/2\omega_0)[1 + j\omega(C_1+C_2)Z_0 - \omega^2C_1C_2Z_0^2]}, \tag{B3}$$

$$S_{21} = \frac{-2\omega^2C_1C_2Z_0^2}{\left[-2\omega^2C_1C_2Z_0^2 + j\omega(C_1+C_2)Z_0\right] + 2(\alpha\lambda/4 + j\pi\Delta/2\omega_0)\left[1 + j\omega(C_1+C_2)Z_0 - \omega^2C_1C_2Z_0^2\right]}, \tag{B4}$$

$$S_{22} = \frac{j\omega(C_1+C_2)Z_0 + 2(\alpha\lambda/4 + j\pi\Delta/2\omega_0)\left[1 + j\omega(C_1-C_2)Z_0 + \omega^2 C_1C_2Z_0^2\right]}{\left[-2\omega^2C_1C_2Z_0^2 + j\omega(C_1+C_2)Z_0\right] + 2(\alpha\lambda/4 + j\pi\Delta/2\omega_0)[1 + j\omega(C_1+C_2)Z_0 - \omega^2C_1C_2Z_0^2]}. \tag{B5}$$

Following a similar procedure in Appendix A, we omit the intermediate steps and obtain the following scattering coefficients:

$$S_{11} \approx \frac{\frac{1}{Q_i} + \frac{2\omega(C_2^2-C_1^2)Z_0}{\pi}}{\left[\frac{1}{Q_i} + \frac{\omega_0^2(C_1^2+C_2^2)Z_0^2}{\pi}\right] + j2\delta}, \quad S_{21} \approx \frac{\frac{-4\omega^2C_1C_2Z_0^2}{\pi}}{\left[\frac{1}{Q_i} + \frac{\omega_0^2(C_1^2+C_2^2)Z_0^2}{\pi}\right] + j2\delta}, \quad S_{22} \approx \frac{\frac{1}{Q_i} + \frac{2\omega(C_1^2-C_2^2)Z_0}{\pi}}{\left[\frac{1}{Q_i} + \frac{\omega_0^2(C_1^2+C_2^2)Z_0^2}{\pi}\right] + j2\delta}. \tag{B6}$$

Here, the resonance frequency is

$$\omega_r = \omega_0 - Z_0\omega_0^2(C_1+C_2)/\pi, \tag{B7}$$

which can be also calculated iteratively.

APPENDIX C: ASYMMETRY IN HANGER-TYPE λ/4 RESONATOR

With circuit asymmetries ΔZ_1 and ΔZ_2, we write the scattering coefficients as

$$\begin{aligned} S_{11} &= \frac{(\Delta z_1 + \Delta z_2)z_3 + (\Delta z_1 - 1)z_2}{(z_1+z_2)z_3 + z_1z_2}, \\ S_{21} = S_{12} &= \frac{2z_3}{(z_1+z_2)z_3 + z_1z_2}, \\ S_{22} &= \frac{(\Delta z_1 + \Delta z_2)z_3 + (\Delta z_2 - 1)z_1}{(z_1+z_2)z_3 + z_1z_2}. \end{aligned} \tag{C1}$$

Here, $\Delta z_1 = \Delta Z_1/Z_0$, $\Delta Z_2 = \Delta Z_2/Z_0$. By defining the external quality factor as $Q'_e = Q_e[1/(2z_1) + 1/(2z_2)]$, we simplify the above relations as

$$S_{11} \approx \left(1 - \frac{2}{z_1+z_2}\right) - \frac{2z_2}{(z_1+z_2)z_1}\frac{Q'_1/Q'_e}{1+2Q'_1\delta}, \tag{C2}$$

$$S_{21} = S_{12} \approx \frac{2}{z_1+z_2}\left(1 - \frac{Q'_1/Q'_e}{1+2Q'_1\delta}\right), \tag{C3}$$

$$S_{22} \approx \left(1 - \frac{2}{z_1+z_2}\right) - \frac{2z_1}{(z_1+z_2)z_2}\frac{Q'_1/Q'_e}{1+2Q'_1\delta}, \tag{C4}$$

where $z_1 = 1 + \Delta z_1$, $z_2 = 1 + \Delta z_2$. For small asymmetries $z_1 \approx z_2 \approx 1$, we obtain the final form of the scattering coefficients described in Eqs. (35)–(37).

APPENDIX D: ASYMMETRY IN NECKLACE-TYPE λ/2 RESONATOR

With circuit asymmetries ΔZ_1 and ΔZ_2, we write the scattering coefficients as

$$S_{11} \approx \frac{[-\omega^2c_1c_2(z_1+z_2-2) + j\omega(c_1+c_2)] + (\alpha l + j\beta l)[-\omega^2c_1c_2z_1z_2 + j\omega(c_1z_1 + c_2z_2) + 1 - 2\omega^2c_1c_2(1-z_2) - 2j\omega c_1]}{[-(z_1+z_2)\omega^2c_1c_2 + j\omega(c_1+c_2)] + (\alpha l + j\beta l)[-z_1z_2\omega^2c_1c_2 + j\omega(z_1c_1 + z_2c_2) + 1 - \omega^2c_1c_2]}, \tag{D1}$$

$$S_{21} = S_{12} \approx \frac{2\omega^2c_1c_2}{[-(z_1+z_2)\omega^2c_1c_2 + j\omega(c_1+c_2)] + (\alpha l + j\beta l)[-z_1z_2\omega^2c_1c_2 + j\omega(z_1c_1 + z_2c_2) + 1 - \omega^2c_1c_2]}, \tag{D2}$$

$$S_{22} \approx \frac{[-\omega^2c_1c_2(z_1+z_2-2) + j\omega(c_1+c_2)] + (\alpha l + j\beta l)[-\omega^2c_1c_2z_1z_2 + j\omega(c_1z_1 + c_2z_2) + 1 - 2\omega^2c_1c_2(1-z_1) - 2j\omega c_2]}{[-(z_1+z_2)\omega^2c_1c_2 + j\omega(c_1+c_2)] + (\alpha l + j\beta l)[-z_1z_2\omega^2c_1c_2 + j\omega(z_1c_1 + z_2c_2) + 1 - \omega^2c_1c_2]}. \tag{D3}$$

Here, we have replaced $\cosh\gamma l$ and $\sinh\gamma l$ by -1 and $-(\alpha l + j\beta l)$, respectively, under the assumption of small loss, and we have defined $c_1 = Z_0C_1$, $c_2 = Z_0C_2$. For small asymmetries $z_1 \approx z_2 \approx 1$ and small coupling capacitances $j\omega Z_0C_1, \omega Z_0C_2 \ll 1$, we simplify the expression as

$$S_{11} \approx \frac{\frac{\pi}{2Q_i} + \omega^2\left(z_2c_2^2 + c_1^2(z_1-2)\right) + j\pi\delta}{\left[\frac{\pi}{2Q_i} + \omega^2\left(z_1c_1^2 + z_2c_2^2\right)\right] + j\pi\delta}, \tag{D4}$$

$$S_{21} = S_{12} \approx \frac{2\omega^2c_1c_2}{\left[\frac{\pi}{2Q_i} + \omega^2\left(z_1c_1^2 + z_2c_2^2\right)\right] + j\pi\delta}, \tag{D5}$$

$$S_{22} \approx \frac{\frac{\pi}{2Q_i} + \omega^2\left(z_1c_1^2 + c_2^2(z_2-2)\right) + j\pi\delta}{\left[\frac{\pi}{2Q_i} + \omega^2\left(z_1c_1^2 + z_2c_2^2\right)\right] + j\pi\delta}. \tag{D6}$$

To proceed, we define $1/Q'_{\rm e} = 1/Q'_{\rm e,1} + 1/Q'_{\rm e,2}$ with $Q'_{\rm e,1} = \pi/2\omega^2 c_1^2 z_1$, $Q'_{\rm e,2} = \pi/2\omega^2 c_2^2 z_2$. The above expression can be simplified as

$$S_{11} \approx 1 - \frac{1}{z_1}\frac{2Q'_{\rm l}/Q'_{\rm e,1}}{1 + j2Q'_{\rm l}\delta},\ S_{21} = S_{12} \approx \frac{1}{\sqrt{z_1 z_2}}\frac{2Q'_{\rm l}/\sqrt{Q'_{\rm e,1}Q'_{\rm e,2}}}{1 + j2Q'_{\rm l}\delta},\ S_{22} \approx 1 - \frac{1}{z_2}\frac{2Q'_{\rm l}/Q'_{\rm e,2}}{1 + j2Q'_{\rm l}\delta}. \tag{D7}$$

For small asymmetries, we omit the phase contributions of $1/z_1$ and $1/z_2$, and obtain the final form of the scattering coefficients described in Eqs. (38)–(40).

APPENDIX E: ASYMMETRY IN CROSS-TYPE λ/2 RESONATOR

With circuit asymmetries ΔZ_1 and ΔZ_2, we write the scattering coefficients as

$$S_{11} = \frac{[j\omega(c_1+c_2) - \omega^2 c_1 c_2(z_1+z_2-2)] + 2(\alpha l + j\pi\Delta/2\omega_0)[1 + j\omega(c_1 z_1 + c_2 z_2) - \omega^2 c_1 c_2 z_1 z_2 + 2\omega^2 c_1 c_2 z_2 - 2j\omega c_1]}{[j\omega(c_1+c_2) - \omega^2 c_1 c_2(z_1+z_2)] + 2(\alpha l + j\pi\Delta/2\omega_0)[1 + j\omega(c_1 z_1 + c_2 z_2) - \omega^2 c_1 c_2 z_1 z_2]}, \tag{E1}$$

$$S_{21} = S_{12} = \frac{-2\omega^2 c_1 c_2}{[j\omega(c_1+c_2) - \omega^2 c_1 c_2(z_1+z_2)] + 2(\alpha l + j\pi\Delta/2\omega_0)[1 + j\omega(c_1 z_1 + c_2 z_2) - \omega^2 c_1 c_2 z_1 z_2]}, \tag{E2}$$

$$S_{22} = \frac{[j\omega(c_1+c_2) - \omega^2 c_1 c_2(z_1+z_2-2)] + 2(\alpha l + j\pi\Delta/2\omega_0)[1 + j\omega(c_1 z_1 + c_2 z_2) - \omega^2 c_1 c_2 z_1 z_2 + 2\omega^2 c_1 c_2 z_1 - 2j\omega c_2]}{[j\omega(c_1+c_2) - \omega^2 c_1 c_2(z_1+z_2)] + 2(\alpha l + j\pi\Delta/2\omega_0)[1 + j\omega(c_1 z_1 + c_2 z_2) - \omega^2 c_1 c_2 z_1 z_2]}. \tag{E3}$$

For small coupling capacitances $j\omega Z_0 C_1, \omega Z_0 C_2 \ll 1$, the above formulas are equivalent to those for a necklace-type $\lambda/2$ resonator, except the π-phase difference in the transmission coefficient. In this regard, the scattering coefficients with small circuit asymmetries are also similar. The complete results are shown in Eqs. (41)–(43) in the main text.

APPENDIX F: CORRECTION OF EXPERIMENTAL IMPERFECTIONS

We now take the necklace-type resonator, shown in Fig. 2(c), as an example and describe a circle-fitting procedure that corrects the experimental imperfections in a practical scattering spectrum. Here, the test data are generated by using a distributed-element circuit model, i.e, ABCD matrices, where the parameters can be fully controlled as a crosscheck of our results. We choose $\alpha = 5.0 \times 10^{-3}$ m^{-1}, $v_{\rm ph} = 1.35 \times 10^8$ m/s, $C_1 = 1.0 \times 10^{-14}$ F, $C_2 = 1.5 \times 10^{-14}$ F, $l = 1.0 \times 10^{-2}$ m, and $Z_0 = 50\ \Omega$ for a necklace-type $\lambda/2$ resonator, which is the same as Fig. 3(b). The resonant frequency is estimated to be $\omega_{\rm r} = 2\pi \times 6.636$ GHz, and the loaded, internal, and external quality factors are $Q_{\rm l} = 1074$, $Q_{\rm i} = 31\,416$, and $Q_{\rm e} = 1112$ with $Q_{\rm e,1} = 3614$ and $Q_{\rm e,2} = 1606$, respectively. Moreover, we consider a small circuit asymmetry on the one side, $\Delta Z_1 = j\omega L_1$ with $L_1 = 1.0 \times 10^{-9}$ H, and two finite-length feedlines with $l_1 = l_2 = 1.2$ m with a 50-Ω impedance match. The simulated reflection coefficient S_{11} is shown in Figs. 5(a) and 5(b). Our correction procedure consists of three major steps.

1. Correction of frequency-dependent phase shift

In the first step, we eliminate the frequency-dependent phase shift $e^{-j(\omega\tau+\varphi_1)}$ with φ_1 being an arbitrary phase offset. This phase shift can be directly seen in Fig. 5(b), where an expected circle of the scattering coefficient is distorted into a knot in the complex plane. We perform the elimination process as follows:

First, we use a linear function to fit τ and φ_1, which serve as an initial guess for a more precise fitting procedure in later steps. The objective function is

$$J_1 = \{-(\omega\tau + \varphi_1) - \arg[S(\omega)]\}^2, \tag{F1}$$

where $\arg[S(\omega)]$ is the unwrapped phase of the complex signal. The fitting result for S_{11} is shown as the red dashed line in Fig. 5(a), where $\tau = 109$ and 214 rad/Hz for S_{11} and S_{22}, respectively.

Next, we use a Lorentzian function to estimate the FWHM, denoted as $\Delta_{\rm 3dB}$, of the line shape, which is used to select data that are close to the resonant frequency. The objective function we use is [44]

$$J_2 = \left(\sqrt{A_1 + \frac{A_2}{1 + 4\left(\frac{\omega-\omega_{\rm r}}{\Delta_{\rm 3dB}}\right)^2}} - |S(\omega)|\right)^2, \tag{F2}$$

where A_1, A_2, $\omega_{\rm r}$, and $\Delta_{\rm 3dB}$ are fitting parameters. The fitting result of S_{11} is shown as the red dashed line in Fig. 5(b), where $\omega_{\rm r} = 2\pi \times 6.637$ GHz and $\Delta_{\rm 3dB} = 2\pi \times 6.24$ MHz. The results for S_{22} are $\omega_{\rm r} = 2\pi \times 6.637$ GHz and $\Delta_{\rm 3dB} = 2\pi \times 6.24$ MHz, which are consistent with S_{11}. The reason to select the data is that the scattering coefficient within the FWHM around the resonant frequency can already form a half-circle in the ideal case, while all the other data form the second half. There exists a huge imbalance in the data volume that influences the fitting result, while we are mostly interested in the data close to the resonant frequency. Moreover, it is preferable to restrict the analysis in a small frequency window in order to minimize the contribution of an uneven background signal. In these regards, we keep only the data within four times of the FWHM, i.e., $|\omega - \omega_{\rm r}| \leqslant 2\Delta_{\rm 3dB}$, for the following steps. We note that these fitted values are rough estimations of the corresponding parameters of a resonator. A more precise characterization will be performed in later steps.

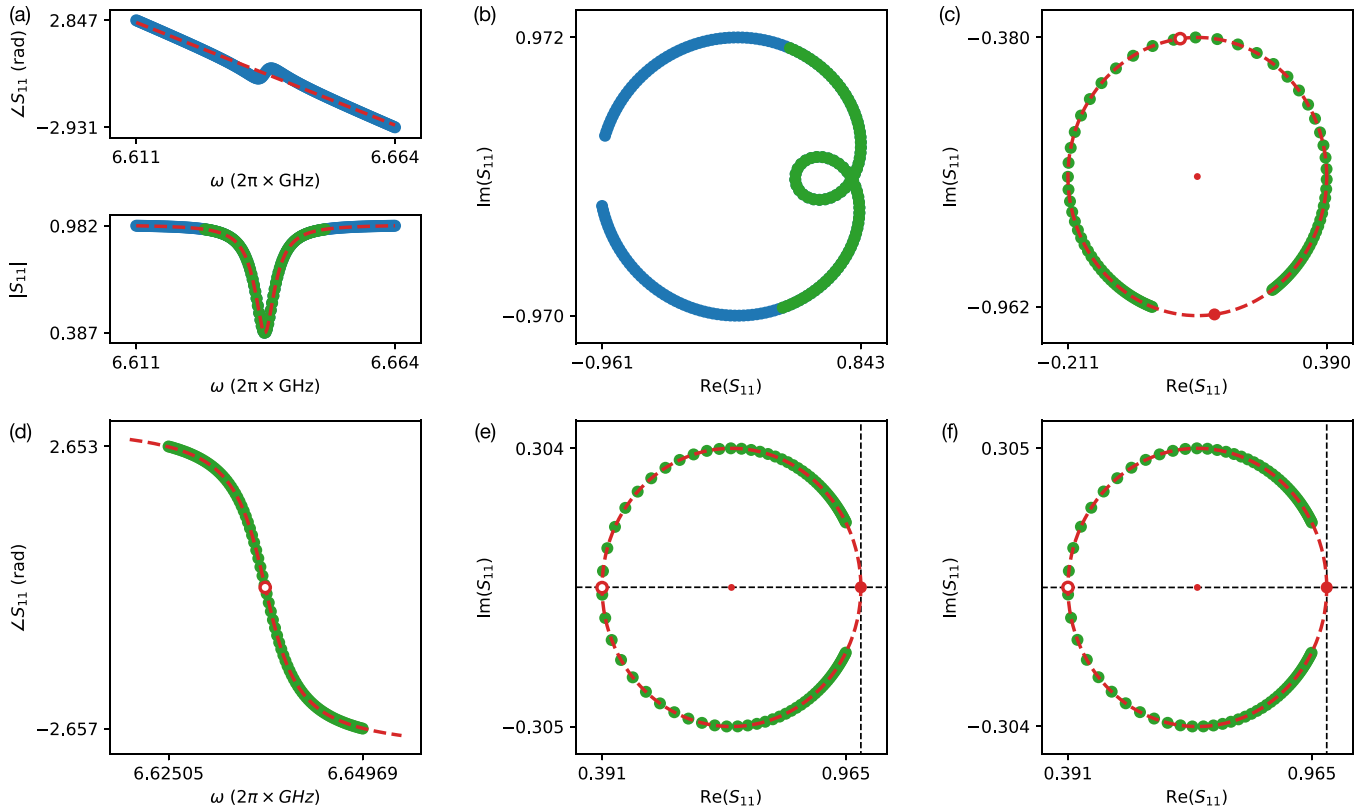

FIG. 5. The step-by-step procedure for removing distortions and characterizing a necklace-type microwave resonator (shown are S_{11} only). (a) Rough phase correction with linear fit and data selection with Lorentzian fit, where the green dots are within ±2 times of FWHM around the estimated resonant frequency. (b) The raw data (blue) and the selected data (green) shown in the complex plane. (c) Fine phase correction with circle fit. (d) Resonant frequency determination with phase versus frequency fit. (e) Correction of cable attenuation and frequency-independent phase. (f) Correction of asymmetry. In all the plots, the fitting results are colored in red. The open and filled red dots represent the scattering coefficients at $|\omega - \omega_r| \to 0$ or $|\omega - \omega_r| \to \infty$, respectively. The small red dot represents the center of the fitted circle.

Having obtained the initial guess of the parameter τ and removed the far off-resonant data points beyond $\omega_r \pm 2\Delta_{3dB}$, we correct the frequency-dependent phase shift by using the circle-fit technique reported in [47]. On the one hand, we use an algebraic method to fit a circle to the phase-corrected scattering coefficients [80], and determine the circle center S_c and the radius r_c. On the other hand, we optimize the parameter τ with the following objective function

$$J_3 = (r_c - |e^{j\omega\tau}S(\omega) - S_{c1}|)^2 \tag{F3}$$

to make the phase-corrected data $S_1(\omega) = e^{j\omega\tau}S(\omega)$ more likely to be a circle. Here, the previously fitted value of τ is used as the initial guess to guarantee the convergence of the optimization algorithm. The corrected data $S_1(\omega)$ and the fitted circle are shown in Fig. 5(c), where $\tau = 111$ rad/Hz and $S_{c1} = -0.448 - j0.520$. The results for S_{22} are $\tau = 113$ rad/Hz and $S_{c1} = 0.334 + j0.036$.

2. Correction of attenuation and frequency-independent phase shift

After correcting the frequency-dependent phase shift $e^{-j(\omega\tau+\varphi_1)}$, the next step is to eliminate the attenuation and the frequency-independent phase shift $Ae^{-j\varphi_2}$ with $\varphi_2 = \varphi - \varphi_1$. We recall the fact that, without the influence of the finite feedline, the reflection coefficient of a necklace-type resonator interacts with the real axis at the reference point $(1 + j0)$ at a far-detuned probe frequency $\omega \to \infty$. We use this property to correct the attenuation and frequency-independent phase shift.

First, we determine the resonant frequency ω_r by using a phase-versus-frequency fit, which is proven to be the most precise and robust fitting method for calibrating a microwave resonator [44]. The objective function is

$$J_4 = \left\{\varphi_2 + 2\arctan\left[2Q_l\left(1 - \frac{\omega}{\omega_r}\right)\right] - \arg\left[S_1(\omega)\right]\right\}^2, \tag{F4}$$

where φ_2, ω_r, and Q_l are fitting parameters. Here, the previously fitted value of ω_r is used as the initial guess to guarantee the convergence of the optimization algorithm. The fitting result of S_{11} is shown in Fig. 5(d), from which we determine the resonant frequency $\omega_r = 2\pi \times 6.637$ GHz and the loaded quality factor $Q_l = 1073$. The results for S_{22} are $\omega_r = 2\pi \times 6.637$ GHz and the loaded quality factor $Q_l = 1052$. These are consistent with the expectation that the loaded quality factor Q_l should not depend on the measurements S_{11} and S_{22}. We determine its value by taking the average $Q_l = 1063$.

Knowing the value of ω_r, one can locate the resonant data point in the fitted circle at $S_{on} = -0.252 - j0.292$. Correspondingly, the far off-resonant point $S_{off} = -0.644 - j0.748$ is determined according to the symmetry of a circle, i.e., $S_{off} = S_{c1} + (S_{c1} - S_{on})$. For S_{22}, we have $S_{on} =$

$-0.317 - j0.0354$ and $S_{\text{off}} = 0.984 + j0.108$. Then, one can correct the attenuation and the frequency-independent phase shift by using the knowledge of the reference point, that is

$$S_2(\omega) = S_1(\omega)/S_{\text{off}}. \tag{F5}$$

The corrected data for S_{11}, which is denoted as $S_2(\omega)$ in the above equation, are shown in Fig. 5(e), where $S_{\text{on}} = 0.391 - j0.001$, $S_{\text{off}} = 1.000 + j0.000$, $S_{c2} = S_{c1}/S_{\text{off}} = -0.696 + j0.000$, $r_{c2} = r_{c1}/|S_{\text{off}}| = 0.304$. For S_{22}, we have $S_{\text{on}} = -0.322 - j0.001$, $S_{\text{off}} = 1.000 + j0.000$, $S_{c2} = S_{c1}/S_{\text{off}} = -0.339 + j0.000$, $r_{c2} = r_{c1}/|S_{\text{off}}| = 0.661$.

3. Correction of circuit asymmetry

After the first two steps, we have removed the influence of the finite feedlines. The last step is to correct the circuit asymmetry. Here, we use the property that the circle center should be located on the real axis in an ideal scattering coefficient. We identify ϕ by the relation

$$\phi = \arg(S_{c2} - S_{\text{off}}) - \pi, \tag{F6}$$

and rotate the circle by $-\phi$ around the reference point $(1 + j0)$. In the meantime, we also rescale the circle radius by a factor of $|\cos\phi|$ to account for the difference between $1/|Q_e|$ and $\text{Re}(1/Q_e)$ [45]. In total, the transformation is described by

$$S_3(\omega) = \cos\phi[S_2(\omega) - 1]e^{-j\phi} + 1. \tag{F7}$$

The corrected reflection coefficient for S_{11}, which is denoted as $S_3(\omega)$ in the above equation, is shown in Fig. 5(f). In this example, we determine $\phi = 0.001$ rad and thus $S_{c3} = 0.696 + j0.000$, $r_{c3} = 0.304$. For S_{22}, we have $\phi = 0.001$ rad and thus $S_{c3} = 0.339 + j0.000$, $r_{c3} = 0.661$. We therefore obtain the two partial external quality factors as, $Q_{e,1} = Q_l/r_{c3} = 3513$ and $Q_{e,2} = Q_l/r_{c3} = 1600$, respectively. The total external quality factor is thus $Q_e = 1099$, and the internal quality factor can be calculated as $Q_i = 33\,070$. Comparing the fitted quality factors Q_l, Q_e, and Q_i with the estimated values, we obtain the relative errors of the calibration results to be 0.9%, 2.3%, and 5.0%, respectively.

[1] X. Gu, A. F. Kockum, A. Miranowicz, Y.-x. Liu, and F. Nori, Microwave photonics with superconducting quantum circuits, Phys. Rep. **718-719**, 1 (2017).

[2] R. J. Schoelkopf and S. M. Girvin, Wiring up quantum systems, Nature (London) **451**, 664 (2008).

[3] D. I. Schuster, A. Wallraff, A. Blais, L. Frunzio, R.-S. Huang, J. Majer, S. M. Girvin, and R. J. Schoelkopf, ac Stark Shift and Dephasing of a Superconducting Qubit Strongly Coupled to a Cavity Field, Phys. Rev. Lett. **94**, 123602 (2005).

[4] A. Wallraff, D. I. Schuster, A. Blais, L. Frunzio, J. Majer, M. H. Devoret, S. M. Girvin, and R. J. Schoelkopf, Approaching Unit Visibility for Control of a Superconducting Qubit with Dispersive Readout, Phys. Rev. Lett. **95**, 060501 (2005).

[5] J. Majer, J. M. Chow, J. M. Gambetta, J. Koch, B. R. Johnson, J. A. Schreier, L. Frunzio, D. I. Schuster, A. A. Houck, A. Wallraff, A. Blais, M. H. Devoret, S. M. Girvin, and R. J. Schoelkopf, Coupling superconducting qubits via a cavity bus, Nature (London) **449**, 443 (2007).

[6] M. A. Sillanpää, J. I. Park, and R. W. Simmonds, Coherent quantum state storage and transfer between two phase qubits via a resonant cavity, Nature (London) **449**, 438 (2007).

[7] M. Hofheinz, E. M. Weig, M. Ansmann, R. C. Bialczak, E. Lucero, M. Neeley, A. D. O'Connell, H. Wang, J. M. Martinis, and A. N. Cleland, Generation of Fock states in a superconducting quantum circuit, Nature (London) **454**, 310 (2008).

[8] M. Hofheinz, H. Wang, M. Ansmann, R. C. Bialczak, E. Lucero, M. Neeley, A. D. O'Connell, D. Sank, J. Wenner, J. M. Martinis, and A. N. Cleland, Synthesizing arbitrary quantum states in a superconducting resonator, Nature (London) **459**, 546 (2009).

[9] L. DiCarlo, J. M. Chow, J. M. Gambetta, L. S. Bishop, B. R. Johnson, D. I. Schuster, J. Majer, A. Blais, L. Frunzio, S. M. Girvin, and R. J. Schoelkopf, Demonstration of two-qubit algorithms with a superconducting quantum processor, Nature (London) **460**, 240 (2009).

[10] L. DiCarlo, M. D. Reed, L. Sun, B. R. Johnson, J. M. Chow, J. M. Gambetta, L. Frunzio, S. M. Girvin, M. H. Devoret, and R. J. Schoelkopf, Preparation and measurement of three-qubit entanglement in a superconducting circuit, Nature (London) **467**, 574 (2010).

[11] J. M. Chow, A. D. Córcoles, J. M. Gambetta, C. Rigetti, B. R. Johnson, J. A. Smolin, J. R. Rozen, G. A. Keefe, M. B. Rothwell, M. B. Ketchen, and M. Steffen, Simple All-Microwave Entangling Gate for Fixed-Frequency Superconducting Qubits, Phys. Rev. Lett. **107**, 080502 (2011).

[12] J. M. Chow, J. M. Gambetta, A. D. Córcoles, S. T. Merkel, J. A. Smolin, C. Rigetti, S. Poletto, G. A. Keefe, M. B. Rothwell, J. R. Rozen, M. B. Ketchen, and M. Steffen, Universal Quantum Gate Set Approaching Fault-Tolerant Thresholds with Superconducting Qubits, Phys. Rev. Lett. **109**, 060501 (2012).

[13] Y. Yin, Y. Chen, D. Sank, P. J. J. O'Malley, T. C. White, R. Barends, J. Kelly, E. Lucero, M. Mariantoni, A. Megrant, C. Neill, A. Vainsencher, J. Wenner, A. N. Korotkov, A. N. Cleland, and J. M. Martinis, Catch and Release of Microwave Photon States, Phys. Rev. Lett. **110**, 107001 (2013).

[14] E. A. Sete, A. Galiautdinov, E. Mlinar, J. M. Martinis, and A. N. Korotkov, Catch-Disperse-Release Readout for Superconducting Qubits, Phys. Rev. Lett. **110**, 210501 (2013).

[15] J. Goetz, S. Pogorzalek, F. Deppe, K. G. Fedorov, P. Eder, M. Fischer, F. Wulschner, E. Xie, A. Marx, and R. Gross, Photon Statistics of Propagating Thermal Microwaves, Phys. Rev. Lett. **118**, 103602 (2017).

[16] J. Goetz, F. Deppe, K. G. Fedorov, P. Eder, M. Fischer, S. Pogorzalek, E. Xie, A. Marx, and R. Gross, Parity-Engineered Light-Matter Interaction, Phys. Rev. Lett. **121**, 060503 (2018).

[17] R. Barends, J. Kelly, A. Megrant, D. Sank, E. Jeffrey, Y. Chen, Y. Yin, B. Chiaro, J. Mutus, C. Neill, P. O'Malley, P. Roushan,

J. Wenner, T. C. White, A. N. Cleland, and J. M. Martinis, Coherent Josephson Qubit Suitable for Scalable Quantum Integrated Circuits, Phys. Rev. Lett. **111**, 080502 (2013).

[18] Y. Chen, C. Neill, P. Roushan, N. Leung, M. Fang, R. Barends, J. Kelly, B. Campbell, Z. Chen, B. Chiaro, A. Dunsworth, E. Jeffrey, A. Megrant, J. Y. Mutus, P. J. J. O'Malley, C. M. Quintana, D. Sank, A. Vainsencher, J. Wenner, T. C. White *et al.*, Qubit Architecture with High Coherence and Fast Tunable Coupling, Phys. Rev. Lett. **113**, 220502 (2014).

[19] E. Jeffrey, D. Sank, J. Y. Mutus, T. C. White, J. Kelly, R. Barends, Y. Chen, Z. Chen, B. Chiaro, A. Dunsworth, A. Megrant, P. J. J. O'Malley, C. Neill, P. Roushan, A. Vainsencher, J. Wenner, A. N. Cleland, and J. M. Martinis, Fast Accurate State Measurement with Superconducting Qubits, Phys. Rev. Lett. **112**, 190504 (2014).

[20] C. Song, K. Xu, W. Liu, C.-p. Yang, S.-B. Zheng, H. Deng, Q. Xie, K. Huang, Q. Guo, L. Zhang, P. Zhang, D. Xu, D. Zheng, X. Zhu, H. Wang, Y.-A. Chen, C.-Y. Lu, S. Han, and J.-W. Pan, 10-Qubit Entanglement and Parallel Logic Operations with a Superconducting Circuit, Phys. Rev. Lett. **119**, 180511 (2017).

[21] C. Song, K. Xu, H. Li, Y.-R. Zhang, X. Zhang, W. Liu, Q. Guo, Z. Wang, W. Ren, J. Hao, H. Feng, H. Fan, D. Zheng, D.-W. Wang, H. Wang, and S.-Y. Zhu, Generation of multicomponent atomic Schrödinger cat states of up to 20 qubits, Science **365**, 574 (2019).

[22] Z. Wang, H. Li, W. Feng, X. Song, C. Song, W. Liu, Q. Guo, X. Zhang, H. Dong, D. Zheng, H. Wang, and D.-W. Wang, Controllable Switching between Superradiant and Subradiant States in a 10-qubit Superconducting Circuit, Phys. Rev. Lett. **124**, 013601 (2020).

[23] Q. Guo, C. Cheng, Z.-H. Sun, Z. Song, H. Li, Z. Wang, W. Ren, H. Dong, D. Zheng, Y.-R. Zhang *et al.*, Observation of energy-resolved many-body localization, Nat. Phys. **17**, 234 (2021).

[24] R. Ma, B. Saxberg, C. Owens, N. Leung, Y. Lu, J. Simon, and D. I. Schuster, A dissipatively stabilized mott insulator of photons, Nature (London) **566**, 51 (2019).

[25] P. Mundada, G. Zhang, T. Hazard, and A. Houck, Suppression of Qubit Crosstalk in a Tunable Coupling Superconducting Circuit, Phys. Rev. Appl. **12**, 054023 (2019).

[26] C. K. Andersen, A. Remm, S. Lazar, S. Krinner, N. Lacroix, G. J. Norris, M. Gabureac, C. Eichler, and A. Wallraff, Repeated quantum error detection in a surface code, Nat. Phys. **16**, 875 (2020).

[27] N. Lacroix, C. Hellings, C. K. Andersen, A. Di Paolo, A. Remm, S. Lazar, S. Krinner, G. J. Norris, M. Gabureac, J. Heinsoo, A. Blais, C. Eichler, and A. Wallraff, Improving the performance of deep quantum optimization algorithms with continuous gate sets, PRX Quantum **1**, 020304 (2020).

[28] J.-C. Besse, K. Reuer, M. C. Collodo, A. Wulff, L. Wernli, A. Copetudo, D. Malz, P. Magnard, A. Akin, M. Gabureac, G. J. Norris, J. I. Cirac, A. Wallraff, and C. Eichler, Realizing a deterministic source of multipartite-entangled photonic qubits, Nat. Commun. **11**, 4877 (2020).

[29] J. Gao, J. Zmuidzinas, B. A. Mazin, H. G. LeDuc, and P. K. Day, Noise properties of superconducting coplanar waveguide microwave resonators, Appl. Phys. Lett. **90**, 102507 (2007).

[30] A. D. O'Connell, M. Ansmann, R. C. Bialczak, M. Hofheinz, N. Katz, E. Lucero, C. McKenney, M. Neeley, H. Wang, E. M. Weig, A. N. Cleland, and J. M. Martinis, Microwave dielectric loss at single photon energies and millikelvin temperatures, Appl. Phys. Lett. **92**, 112903 (2008).

[31] C. Song, T. W. Heitmann, M. P. DeFeo, K. Yu, R. McDermott, M. Neeley, J. M. Martinis, and B. L. T. Plourde, Microwave response of vortices in superconducting thin films of re and al, Phys. Rev. B **79**, 174512 (2009).

[32] C. Song, M. P. DeFeo, K. Yu, and B. L. T. Plourde, Reducing microwave loss in superconducting resonators due to trapped vortices, Appl. Phys. Lett. **95**, 232501 (2009).

[33] J. Gao, L. R. Vale, J. A. B. Mates, D. R. Schmidt, G. C. Hilton, K. D. Irwin, F. Mallet, M. A. Castellanos-Beltran, K. W. Lehnert, J. Zmuidzinas, and H. G. Leduc, Strongly quadrature-dependent noise in superconducting microresonators measured at the vacuum-noise limit, Appl. Phys. Lett. **98**, 232508 (2011).

[34] J. M. Sage, V. Bolkhovsky, W. D. Oliver, B. Turek, and P. B. Welander, Study of loss in superconducting coplanar waveguide resonators, J. Appl. Phys. **109**, 063915 (2011).

[35] A. Megrant, C. Neill, R. Barends, B. Chiaro, Y. Chen, L. Feigl, J. Kelly, E. Lucero, M. Mariantoni, P. J. J. O'Malley, D. Sank, A. Vainsencher, J. Wenner, T. C. White, Y. Yin, J. Zhao, C. J. Palmstrøm, J. M. Martinis, and A. N. Cleland, Planar superconducting resonators with internal quality factors above one million, Appl. Phys. Lett. **100**, 113510 (2012).

[36] K. Geerlings, S. Shankar, E. Edwards, L. Frunzio, R. J. Schoelkopf, and M. H. Devoret, Improving the quality factor of microwave compact resonators by optimizing their geometrical parameters, Appl. Phys. Lett. **100**, 192601 (2012).

[37] A. Bruno, G. de Lange, S. Asaad, K. L. van der Enden, N. K. Langford, and L. DiCarlo, Reducing intrinsic loss in superconducting resonators by surface treatment and deep etching of silicon substrates, Appl. Phys. Lett. **106**, 182601 (2015).

[38] J. Goetz, F. Deppe, M. Haeberlein, F. Wulschner, C. W. Zollitsch, S. Meier, M. Fischer, P. Eder, E. Xie, K. G. Fedorov, E. P. Menzel, A. Marx, and R. Gross, Loss mechanisms in superconducting thin film microwave resonators, J. Appl. Phys. **119**, 015304 (2016).

[39] L. Frunzio, A. Wallraff, D. Schuster, J. Majer, and R. Schoelkopf, Fabrication and characterization of superconducting circuit QED devices for quantum computation, IEEE Trans. Appl. Supercond. **15**, 860 (2005).

[40] M. Göppl, A. Fragner, M. Baur, R. Bianchetti, S. Filipp, J. M. Fink, P. J. Leek, G. Puebla, L. Steffen, and A. Wallraff, Coplanar waveguide resonators for circuit quantum electrodynamics, J. Appl. Phys. **104**, 113904 (2008).

[41] H. Wang, A. P. Zhuravel, S. Indrajeet, B. G. Taketani, M. D. Hutchings, Y. Hao, F. Rouxinol, F. K. Wilhelm, M. D. LaHaye, A. V. Ustinov, and B. L. T. Plourde, Mode Structure in Superconducting Metamaterial Transmission-Line Resonators, Phys. Rev. Appl. **11**, 054062 (2019).

[42] M. Castellanos-Beltran, Development of a josephson parametric amplifier for the preparation and detection of nonclassical states of microwave fields, Ph.D. thesis, University of Colorado Boulder, 2010.

[43] J. Braumuller, Quantum simulation experiments with superconducting circuits, Ph.D. thesis, KIT, 2018.

[44] P. J. Petersan and S. M. Anlage, Measurement of resonant frequency and quality factor of microwave resonators: Comparison of methods, J. Appl. Phys. **84**, 3392 (1998).

[45] M. S. Khalil, M. J. A. Stoutimore, F. C. Wellstood, and K. D. Osborn, An analysis method for asymmetric resonator transmission applied to superconducting devices, J. Appl. Phys. **111**, 054510 (2012).

[46] C. Deng, M. Otto, and A. Lupascu, An analysis method for transmission measurements of superconducting resonators with applications to quantum-regime dielectric-loss measurements, J. Appl. Phys. **114**, 054504 (2013).

[47] S. Probst, F. B. Song, P. A. Bushev, A. V. Ustinov, and M. Weides, Efficient and robust analysis of complex scattering data under noise in microwave resonators, Rev. Sci. Instrum. **86**, 024706 (2015).

[48] C. R. H. McRae, H. Wang, J. Gao, M. R. Vissers, T. Brecht, A. Dunsworth, D. P. Pappas, and J. Mutus, Materials loss measurements using superconducting microwave resonators, Rev. Sci. Instrum. **91**, 091101 (2020).

[49] J.-H. Yeh and S. M. Anlage, In situ broadband cryogenic calibration for two-port superconducting microwave resonators, Rev. Sci. Instrum. **84**, 034706 (2013).

[50] L. Ranzani, L. Spietz, Z. Popovic, and J. Aumentado, Two-port microwave calibration at millikelvin temperatures, Rev. Sci. Instrum. **84**, 034704 (2013).

[51] G. Cataldo, E. J. Wollack, E. M. Barrentine, A. D. Brown, S. H. Moseley, and K. U-Yen, Analysis and calibration techniques for superconducting resonators, Rev. Sci. Instrum. **86**, 013103 (2015).

[52] Q.-M. Chen, M. Partanen, F. Fesquet, K. E. Honasoge, F. Kronowetter, Y. Nojiri, M. Renger, K. G. Fedorov, A. Marx, F. Deppe, and R. Gross, Scattering coefficients of superconducting microwave resonators. II. System-bath approach, Phys. Rev. B **106**, 214506 (2022).

[53] D. M. Pozar, *Microwave Engineering (4th ed.)* (Wiley, Hoboken, NJ, 2011).

[54] H. Paik, D. I. Schuster, L. S. Bishop, G. Kirchmair, G. Catelani, A. P. Sears, B. R. Johnson, M. J. Reagor, L. Frunzio, L. I. Glazman, S. M. Girvin, M. H. Devoret, and R. J. Schoelkopf, Observation of High Coherence in Josephson Junction Qubits Measured in a Three-Dimensional Circuit QED Architecture, Phys. Rev. Lett. **107**, 240501 (2011).

[55] C. Rigetti, J. M. Gambetta, S. Poletto, B. L. T. Plourde, J. M. Chow, A. D. Córcoles, J. A. Smolin, S. T. Merkel, J. R. Rozen, G. A. Keefe, M. B. Rothwell, M. B. Ketchen, and M. Steffen, Superconducting qubit in a waveguide cavity with a coherence time approaching 0.1 ms, Phys. Rev. B **86**, 100506(R) (2012).

[56] T. Brecht, M. Reagor, Y. Chu, W. Pfaff, C. Wang, L. Frunzio, M. H. Devoret, and R. J. Schoelkopf, Demonstration of superconducting micromachined cavities, Appl. Phys. Lett. **107**, 192603 (2015).

[57] T. Brecht, W. Pfaff, C. Wang, Y. Chu, L. Frunzio, M. H. Devoret, and R. J. Schoelkopf, Multilayer microwave integrated quantum circuits for scalable quantum computing, npj Quantum Inf. **2**, 16002 (2016).

[58] T. Brecht, Y. Chu, C. Axline, W. Pfaff, J. Z. Blumoff, K. Chou, L. Krayzman, L. Frunzio, and R. J. Schoelkopf, Micromachined Integrated Quantum Circuit Containing a Superconducting Qubit, Phys. Rev. Appl. **7**, 044018 (2017).

[59] E. Xie, F. Deppe, M. Renger, D. Repp, P. Eder, M. Fischer, J. Goetz, S. Pogorzalek, K. G. Fedorov, A. Marx, and R. Gross, Compact 3d quantum memory, Appl. Phys. Lett. **112**, 202601 (2018).

[60] L. V. Abdurakhimov, I. Mahboob, H. Toida, K. Kakuyanagi, and S. Saito, A long-lived capacitively shunted flux qubit embedded in a 3d cavity, Appl. Phys. Lett. **115**, 262601 (2019).

[61] A. Romanenko, A. Grassellino, A. C. Crawford, D. A. Sergatskov, and O. Melnychuk, Ultra-high quality factors in superconducting niobium cavities in ambient magnetic fields up to 190 mg, Appl. Phys. Lett. **105**, 234103 (2014).

[62] A. Romanenko, R. Pilipenko, S. Zorzetti, D. Frolov, M. Awida, S. Belomestnykh, S. Posen, and A. Grassellino, Three-Dimensional Superconducting Resonators at $t < 20$ mk with Photon Lifetimes up to $\tau = 2$ s, Phys. Rev. Appl. **13**, 034032 (2020).

[63] C. U. Lei, L. Krayzman, S. Ganjam, L. Frunzio, and R. J. Schoelkopf, High coherence superconducting microwave cavities with indium bump bonding, Appl. Phys. Lett. **116**, 154002 (2020).

[64] S. Chakram, A. E. Oriani, R. K. Naik, A. V. Dixit, K. He, A. Agrawal, H. Kwon, and D. I. Schuster, Seamless High-q Microwave Cavities for Multimode Circuit Quantum Electrodynamics, Phys. Rev. Lett. **127**, 107701 (2021).

[65] M. Reagor, H. Paik, G. Catelani, L. Sun, C. Axline, E. Holland, I. M. Pop, N. A. Masluk, T. Brecht, L. Frunzio, M. H. Devoret, L. Glazman, and R. J. Schoelkopf, Reaching 10 ms single photon lifetimes for superconducting aluminum cavities, Appl. Phys. Lett. **102**, 192604 (2013).

[66] M. Reagor, W. Pfaff, C. Axline, R. W. Heeres, N. Ofek, K. Sliwa, E. Holland, C. Wang, J. Blumoff, K. Chou, M. J. Hatridge, L. Frunzio, M. H. Devoret, L. Jiang, and R. J. Schoelkopf, Quantum memory with millisecond coherence in circuit QED, Phys. Rev. B **94**, 014506 (2016).

[67] M. Kudra, J. Biznárová, A. F. Roudsari, J. J. Burnett, D. Niepce, S. Gasparinetti, B. Wickman, and P. Delsing, High quality three-dimensional aluminum microwave cavities, Appl. Phys. Lett. **117**, 070601 (2020).

[68] H. Wang, S. Singh, C. R. H. McRae, J. C. Bardin, S.-X. Lin, N. Messaoudi, A. R. Castelli, Y. J. Rosen, E. T. Holland, D. P. Pappas, and J. Y. Mutus, Cryogenic single-port calibration for superconducting microwave resonator measurements, Quantum Sci. Technol. **6**, 035015 (2021).

[69] Z. K. Minev, I. M. Pop, and M. H. Devoret, Planar superconducting whispering gallery mode resonators, Appl. Phys. Lett. **103**, 142604 (2013).

[70] Z. K. Minev, K. Serniak, I. M. Pop, Z. Leghtas, K. Sliwa, M. Hatridge, L. Frunzio, R. J. Schoelkopf, and M. H. Devoret, Planar Multilayer Circuit Quantum Electrodynamics, Phys. Rev. Appl. **5**, 044021 (2016).

[71] B. Mazin, Microwave kinetic inductance detectors, Ph.D. thesis, California Institute of Technology, 2004.

[72] J. Gao, The physics of superconducting microwave resonators, Ph.D. thesis, California Institute of Technology, 2008.

[73] M. Jerger, Experiments on superconducting qubits coupled to resonators, Ph.D. thesis, KIT, 2013.

[74] K. Geerlings, Improving coherence of superconducting qubits and resonators, Ph.D. thesis, Yale University, 2013.

[75] M. J. Reagor, Superconducting cavities for circuit quantum electrodynamics, Ph.D. thesis, Yale University, 2015.

[76] D. Schuster, Circuit quantum electrodynamics, Ph.D. thesis, Yale University, 2007.
[77] M. V. Göppl, Engineering quantum electronic chips, Ph.D. thesis, ETH Zürich, 2009.
[78] M. Fischer, Q.-M. Chen, C. Besson, P. Eder, J. Goetz, S. Pogorzalek, M. Renger, E. Xie, M. J. Hartmann, K. G. Fedorov, A. Marx, F. Deppe, and R. Gross, In situ tunable nonlinearity and competing signal paths in coupled superconducting resonators, Phys. Rev. B **103**, 094515 (2021).
[79] https://github.com/chenqmion/ScatteringCoe.
[80] N. Chernov and C. Lesort, Least squares fitting of circles, J. Math. Imaging Vis. **23**, 239 (2005).